

FRETtranslator: translating FRET traces into RNA structural pathways

Nikolai Hecker^{1, 2}, Matthew Kahlscheuer³, Peter Kerpedjiev⁵, Jan Gorodkin^{1, 2}, Peter F. Stadler^{1, 5-10}, Ivo L. Hofacker^{1, 5, 6}, Nils Walter^{3*}, Jing Qin^{1, 5, 11*}

1 Center for non-coding RNA in Technology and Health

2 Department of Veterinary Clinical and Animal Sciences, University of Copenhagen, Grønnegårdsvej 3, 1870 Frederiksberg C, Denmark

3 Single Molecule Analysis Group, Center for RNA Biomedicine, Department of Chemistry, University of Michigan, Ann Arbor, USA

4 Centre for Bioinformatics, University of Hamburg, Bundesstr. 43, 20146 Hamburg

5 Institute for Theoretical Chemistry, Univ. Vienna, Währingerstr. 17, 1090 Vienna, Austria

6 Research group BCB, Faculty of Computer Science, Univ. Vienna, Austria

7 Dept. of Computer Science & IZBI & iDiv & LIFE, Leipzig Univ., Härtelstr. 16-18, Leipzig, Germany

8 Max Planck Institute for Mathematics in the Sciences, Inselstr. 22, Leipzig, Germany

9 Fraunhofer Institute IZI, Perlickstr. 1, Leipzig, Germany

10 Santa Fe Institute, 1399 Hyde Park Rd., Santa Fe, NM87501, USA

11 IMADA, Univ. Southern Denmark, Campusvej 55, Odense, Denmark.

* qin@tbi.univie.ac.at (JQ); nwalter@umich.edu (NGW)

Abstract

Recent genome and transcriptome sequencing projects have unveiled a plethora of highly structured RNA molecules as central mediators of cellular function. Single-molecule Förster Resonance Energy Transfer (smFRET) is a powerful tool for analyzing the temporal evolution of the full structure of individual RNA molecules, in pursuit of understanding their essential structure-dynamics-function relationships. In contrast to enzymatic and chemical footprinting, NMR spectroscopy and X-ray crystallography, smFRET yields temporally resolved, quantitative information about single molecules rather than only time and ensemble averages of entire populations. This makes unique observations of transient and rare conformations under both equilibrium and non-equilibrium conditions possible. However, the structural information obtained is limited to a one-dimensional (1D) distance between pairs of fluorophore labeling sites as a projection of a molecule's 3D structure. It therefore remains an unmet challenge to relate smFRET data back to the underlying temporal sequence of transitions between RNA 3D structures. Here, we describe a hidden Markov model approach to translate smFRET time traces into the most probable corresponding secondary structure paths on the folding free energy landscape of the RNA. This is achieved by combining predictions from the RNA's folding landscape and 3D structure into a computational framework termed **FRETtranslator**. **FRETtranslator** predicts RNA secondary structure transitions solely based on the RNA sequence and an input smFRET trace. Application of **FRETtranslator** to a preQ₁-riboswitch successfully recapitulates its reversible transitions between hairpin and pseudoknot structures. To our knowledge, **FRETtranslator** is the first computational tool that provides a direct structural interpretation of smFRET data for RNA. It is

freely available at <http://sourceforge.net/projects/FRETtranslator/> under terms of the GNU General Public License v3.0.

Author Summary

Understanding how an RNA sequence folds is becoming increasingly important as our understanding of the diverse functions of RNA is continuously expanding. Measurements using single-molecule Förster resonance energy transfer (smFRET) have yielded unprecedented kinetic and mechanistic insights into RNA folding and conformational changes. However, observations from smFRET experiments are limited to a time series of inter-fluorophore distances between two specific, pre-determined labeling sites that reflect but also hide many details of the underlying RNA structures and folding pathways. Here, we present **FRETtranslator**, a hidden Markov model approach that predicts the most likely time series of RNA secondary structure transitions underlying a given smFRET trace. **FRETtranslator** combines the smFRET-derived inter-fluorophore distance information with coarse-grained modeling of both the folding free energy landscape and resulting 3D structures of the RNA. We applied **FRETtranslator** to smFRET data for a 36-nt transcriptional preQ₁ riboswitch from *Bacillus subtilis* (*Bsu*) to predict the temporal sequences of secondary structures underlying their equilibrium folding transitions. **FRETtranslator** is freely available at <http://sourceforge.net/projects/FRETtranslator/>.

Introduction

Key cellular processes involving the maintenance, modification, and regulated expression of the genome critically depend on the ability of RNA to fold into specific structures that are sufficiently dynamic to undergo rearrangements that are necessary for their function. For instance, bacterial riboswitches change their conformation upon ligand binding, leading to an altered level of transcription or translation [1–4]; RNA thermometers harness structural rearrangements to affect temperature-induced changes in gene expression [5]; catalytic RNAs utilize magnesium-dependent changes in structure to gate catalysis [6, 7]; and the efficient biosynthesis of viable messenger (m)RNAs relies on guided conformational rearrangements of the pre-mRNA substrate of the spliceosome [8–10].

Since the functions of these non-coding RNAs intrinsically tied to such structural rearrangements, it is important to determine and further investigate these structural changes and their folding kinetics. Extensive experimental and computational studies on RNA folding have provided significant insights into the kinetic mechanism of RNA functions, see [11] and references therein.

Experimental approaches such as RNA footprinting or spectroscopy [12, 13], have been developed to incorporate structural constraints in order to improve the accuracy for predicting RNA native structures. Both base-paired and unpaired nucleotides can be more accurately defined [14, 15]. However, due to their inherent ensemble- and time-averaging, both footprinting and NMR spectroscopy typically obtain ambiguous or ill-defined data for dynamic RNAs, which cannot easily be deconvolved into the constituent time series of individual RNA structures.

Single-molecule fluorescence resonance energy transfer (smFRET) [16] microscopy has become an increasingly popular tool to study the structural dynamics of RNA molecules. It reveals, in real time, the structural dynamics of these molecules by monitoring the distance between two dye-labeled atoms of an RNA molecule. Unlike ensemble structure probing, smFRET reveals events occurring transiently and in small numbers of individual molecules both at and far from equilibrium. It provides information about subpopulations

with distinct behaviors and can detect even subtle changes in folding kinetics that alter RNA tertiary or secondary structure. Hence, smFRET has been successfully used to characterize the role of dynamics in functional RNAs and their protein complexes, including riboswitches, ribozymes, the ribosome, and the spliceosome [1, 2, 6, 9, 17–19].

Previous computational analyses of smFRET time traces have typically focused on characterizing the idealized FRET states and estimating the transition rates between them [20, 21]. Associating specific structures with these states, however, remains a challenging task and often requires arbitrary choices and/or expensive and time-consuming control experiments. For example, a sophisticated hidden Markov model (HMM) based approach was used to study smFRET traces of a Diels-Alderase ribozyme [22]. The derived transition states were assigned to separately predicted RNA secondary structures. Consequently, the association of FRET states with secondary structures was not an intrinsic part of the model, but based on the authors' interpretation. A separate set of computational tools was developed for the simulation of tertiary structures. For instance, the 36-nucleotide (nt) transcriptional *Bacillus subtilis* (*Bsu*) riboswitch with a known crystal structure was studied with two coarse-grained molecular dynamics simulation approaches, termed TOPRNA and Gō models [19, 23]. In the former approach, predicted mean distances between the fluorophores were compared to measured smFRET efficiencies to assign a most likely structural model to a FRET state. However, molecular simulations of RNA usually require extensive a priori knowledge of the structure under investigation, e.g., a crystal structure [24]. Without such prior knowledge, molecular simulations rely on an accurate prediction of the tertiary structure, which is notoriously unreliable in the absence of experimental input, given the rugged folding landscapes of RNAs [25, 26]. A recently developed method, multidimensional Chemical Mapping (MCM) [27] provides a means of disentangling structural alternatives but lacks temporal information. At present MCM appears to be limited to abundant states, however.

Compared to these approaches, **FRETtranslator**'s advantage is that it predicts RNA secondary structure transitions based on *solely* the RNA sequence and smFRET traces. **FRETtranslator** employs an HMM approach to "translate" each input smFRET trace independently to a time series of specific RNA conformational changes. The state space for this HMM is a particular set of secondary structures in a coarse-grained model of the RNA folding landscape known as the basin hopping graph (BHG) [28]. The transition probabilities between two states are evaluated computationally according to their corresponding energy barrier within the BHG framework as well. The emission states are grouped FRET values extracted from input smFRET traces. In the current study, input smFRET traces are idealized with well-established HMM software such as vbFRET [20] and QuB [21]. The emission probability of a given secondary structure is inferred from an empirical distribution of inter-fluorophore distances by applying the Förster equation. This empirical inter-fluorophore distance distribution is simulated with software **Ernwin** [29], which is able to efficiently sample 3D structures satisfying an input secondary structure.

In the following, we refer to the resulting HMM as *BHG-HMM* to distinguish it from the HMMs used in idealizing the smFRET input traces. To validate our method, we show that our predicted structural transitions for the *Bsu* riboswitch example are consistent with those from previous TOPRNA modeling of similar smFRET data [19].

Materials and Methods

BHG-HMM Construction

Hidden states, initial and transition probabilities from RNA folding landscapes

We first briefly review the relevant concepts of the RNA folding landscape and the BHG approach. For details, we refer to [28,30,31] and S1 Text.

Given an RNA sequence, we consider the underlying structural space as the set of all secondary structures that can be formed by this sequence assuming that 1) only canonical (GC, AU, and GU) base pairs are formed; 2) hairpin loops have a minimum length of three; and 3) particular types of pseudoknots defined in [32] can be included. These conditions define the ensemble of structures as implemented in the most commonly used RNA folding tools such as *Mfold* [33] and the *ViennaRNA* package [34].

The (free) energy $f(x)$ of each structure x in this ensemble is evaluated following well-established energy models [35,36] in the form of additive contributions for base pair stacking as well as hairpin loops, interior loops, bulges and multi-loops. RNA structures in the underlying structural space are arranged as a graph by specifying which pair of structures can be interconverted with elementary rearrangements, typically the opening or closing of individual base pairs. This graph is referred to as the *landscape* in the following.

The size of the underlying space grows exponentially according to the RNA sequence length [37]. The coarse-grained basin hopping graph (BHG) model was introduced in [28] to alleviate this combinatorial explosion and allow an efficient investigation of the folding dynamic of RNAs of moderate lengths. Nodes in the BHG represent secondary structures that are locally stable. More precisely, the folding energy of a structure that qualifies as a BHG node is strictly smaller than the energies of all neighbor structures in the landscape. We refer to such a structure as a *local minimum (LM)*. Two LMs in the BHG are linked by an edge if the direct transition between them is "energetically favourable", i.e., introducing any detour in the landscape between these two LMs does not further lower the energy required for the molecule to complete the conformational conversion. The weight on each edge indicates the energy barrier for converting two adjacent LMs. As a result, optimal folding pathways are modeled as paths in the BHG represented by their LMs.

FRETtranslator uses the resulting BHG to obtain the hidden states, initial and transition probabilities. The hidden states are the LMs in the BHG, which we refer to as *candidate structures*. The initial probabilities for the candidate structures are estimated from their Boltzmann weights. To be precise, for a candidate structure x with free energy $f(x)$, its initial probability is

$$\frac{e^{-f(x)/RT}}{\sum_{s \in \mathcal{X}} e^{-f(s)/RT}},$$

where the denominator sums over the set \mathcal{X} of all candidate structures taking into consideration. We further describe the dynamics among candidate structures as a continuous-time Markov process. Assume there are in total N candidate structures, transition probabilities between pairs of candidate structures for each time period t are then computed by numerically computing the matrix exponential $\exp(t\mathbf{M})$ where $\mathbf{M} = (r_{yx})$ is the $N \times N$ infinitesimal generator matrix [30]. In which, r_{yx} denotes the transition rate from a candidate structure x to another candidate structure y . This rate is nonzero only if x and y are connected by exactly one edge in the BHG. In this case, according to the Metropolis rule,

$$r_{yx} = c_0 \cdot e^{-(S(x,y)-f(x))} \quad (1)$$

$S(x, y)$ is the edge weight between x and y in BHG, $f(x)$ evaluates the energy of x , R is the universal gas constant, \mathcal{T} is the absolute ambient temperature. The parameter c_0 gauges the time axis and will be referred to as *time-scalar* in the following. It collects entropic terms that cannot be computed directly from the landscape in our setting and depends to a certain extent on the particular given RNA sequence. We treat this time scalar c_0 as a user-defined parameter. In our experience, a default value of 100 is useful as a first trial when the unit time is 0.1s (see Result section). Such default value assumes that in 0.1s the molecule experiences about 100 basin-hoppings in its landscape.

Emission states and estimations of emission probabilities based on 3D RNA sampling

The FRET (efficiency) values will be used as the emission states of our BHG-HMM. To reduce the influence of noise from the smFRET measurements, we use idealized smFRET traces as input, i.e., traces that are pre-processed with software such as vbFRET [20] or QuB [21]. These programs allow for the application of HMM algorithms to smFRET trajectories, and the extraction of idealized FRET states and rate constants of their interconversion. Also, these HMM programs currently present the most accessible form of data analysis that produces the most reliable results with minimal a priori assumptions required from the user [38].

More precisely, with a user-defined parameter b , all nonzero FRET values are partitioned into b emission states: $(0, 1/b], \dots, (1 - 1/b, 1]$. In the following, we refer to these emission states as bins. For instance, $b = 5$ indicates the FRET values grouped into five emission states $(0, 0.2]$, $(0.2, 0.4]$, $(0.4, 0.6]$, $(0.6, 0.8]$ and $(0.8, 1]$. We also use an additional bin to accommodate extreme situations like “no signal” or missing data.

To estimate the emission probabilities, as exemplified by Fig. 1 (A), **FRETtranslator** utilizes the following procedure. First, for each candidate structure, a set of 3D structures that satisfies the constraints implied by the candidate secondary structure is generated using **Ernwin** [29]. We will refer to these sampled 3D structures as *in silico* 3D structures. Next, we estimate *in silico* the distance d between the locations where two fluorophores are located in each *in silico* 3D structure. This yields the inter-fluorophore distance distribution for each candidate structure, which is further converted into the distribution of FRET values E_{FRET} of the candidate structure according to the following Förster equation [39]:

$$E_{FRET} = ((1 + (d/R_0)^6))^{-1}. \quad (2)$$

Here, R_0 is the Förster radius, i.e., the distance between the fluorophores corresponding to 50% FRET efficiency. In **FRETtranslator**, we use a default value of $R_0 = 54$ Å when the cyanine dyes Cy3 and Cy5 fluorophores are used [19, 40].

As mentioned above, all *in silico* 3D structures are sampled with **Ernwin**, a coarse-grain helix-centered model that allows one to rapidly sample a set of 3D structures satisfying a given secondary structure. Because of its coarse-graining nature, on one hand, **Ernwin** samples the conformational space more efficiently than approaches based on all-atom models such as the Rosetta software suite [41]. Therefore, sufficient samplings of *in silico* 3D structures can be derived for larger RNA molecules. On the other hand, inter-fluorophore distances measured by **Ernwin** are approximations of distances between coarse-grain structural elements where the fluorophores are located. For more details regarding this approximation, see S2 Text.

Therefore, we assume that certain inaccuracies can exist in the **Ernwin**-estimated distribution of inter-fluorophore distances and the resulting emission probabilities. To address this inaccuracy, noise at different levels is added to “perturb” both the derived distribution of inter-fluorophore distances and the structural transition results predicted

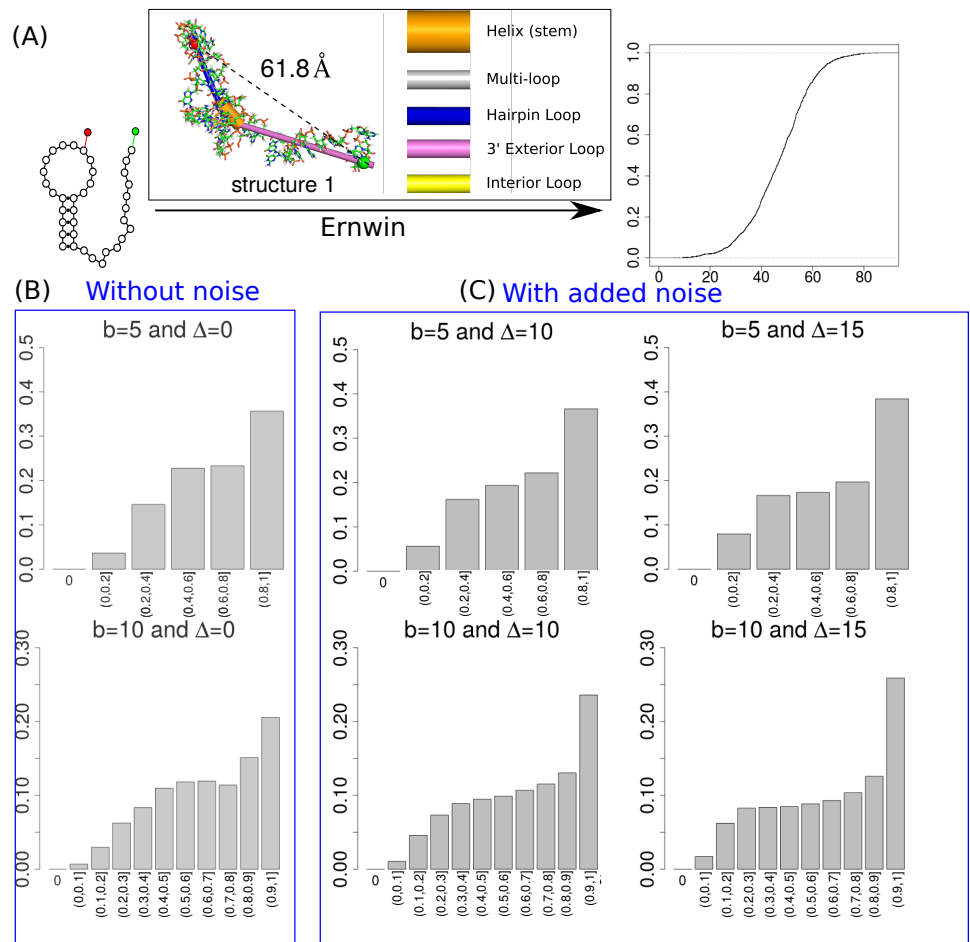


Fig 1. Estimating emission probabilities of a candidate structure. (A) Once a candidate structure is found, *Ernwin* [29] is used to generate a set of *in silico* 3D structures satisfying the structural constraints implied by this candidate structure. An exemplary 3D structure is shown above the arrow with structural elements indicated in the legend. Afterwards, the inter-fluorophore distance distribution is collected from this set of *in silico* 3D structures. The empirical cumulative distribution of the example candidate structure is shown to the right of the arrow. This inter-fluorophore distance distribution is then converted to a distribution of FRET values according to the Förster equation. (B) Finally, grouping FRET values into b bins derives emission probabilities as shown in the histograms. Each bar indicates the emission probability of a bin and is labeled by the interval of FRET values that the corresponding bin contains. (C) This derived distribution of emission probabilities can be perturbed by adding noise at a defined level as described in more detail at the end of this section. The number of bins and the noise level are user-defined parameters. In this figure, we set the number of bins b to either 5 or 10 and the noise level Δ to 10 or 15 Å.

with *FRETtranslator*. Only predictions robust against this added noise are taken into consideration.

More particularly, for each inter-fluorophore distance d obtained with *Ernwin*, 100 random noise values within a user defined range $(d - \Delta, d + \Delta)$ are added to the original *Ernwin* derived data. These random values are generated following by default a uniform distribution. In Fig. 1 (B), we show an example of emission probabilities estimated

without and with added noise. Noise generated by other distributions, for instance a Gaussian distribution, can be handled analogously. The user-defined range Δ is referred to as *noise level* throughout the remainder of this contribution. When no noise is added, we simply write $\Delta = 0$.

The Viterbi algorithm

For a given RNA molecule, BHG-HMMs used in **FRETtranslator** can be constructed based on BHG and **Ernwin**-sampled distances as described above. The resulting model includes the following information: a set S of candidate structures, initial probabilities $\pi(s_1)$ for starting from the candidate structure s_1 , transition probabilities $\alpha(s_i, s_j)$ of transitioning from candidate structure s_i to s_j , and emission probabilities $\beta(F_k|s_i)$ that one observes a FRET value within bin F_k given a candidate structure s_i . In which, F_k is one of the b bins mentioned above.

Assume a BHG-HMM is fixed and an input FRET trace with FRET values of length T (time steps), denoted by f_1, f_2, \dots, f_T , is given. **FRETtranslator** first converts each FRET value f_t to its corresponding bin F_t , where $1 \leq t \leq T$. Then the likelihood function for a sequence of candidate structures s_1, s_2, \dots, s_T that produces this FRET trace is computed in the following:

$$\begin{aligned} & \mathbb{P}(s_1, s_2, \dots, s_T | F_1, F_2, \dots, F_T) \\ = & \pi(s_1) \cdot \beta(F_1 | s_1) \cdot \alpha(s_1, s_2) \cdot \beta(F_2 | s_2) \cdot \dots \cdot \beta(F_{T-1} | s_{T-1}) \cdot \alpha(s_{T-1}, s_T) \cdot \beta(F_T | s_T). \end{aligned}$$

The most likely sequence of candidate structures x_1, x_2, \dots, x_T is thus the one that maximizes this likelihood. We refer to the logarithm of this maximal likelihood as the *Viterbi score* of this input FRET trace under the specific BHG-HMM architecture. The Viterbi score of this BHG-HMM is defined as the sum of the Viterbi scores over all input traces.

The Viterbi algorithm [42] derives the optimal sequence of candidate structures with time complexity $O(T \cdot |S|^2)$ in dynamic programming manner, where T is the length of the FRET trace and $|S|$ is the total number of candidate structures taken into consideration.

FRETtranslator implementation details

FRETtranslator employs StochHMM [43] for the Viterbi-decoding. **FRETtranslator** provides a collection of Perl, R and BASH scripts that are compliant with Linux and most UNIX-like systems for analyzing pre-processed smFRET traces.

Parameter selection and robustness analysis in the *Bacillus subtilis* preQ₁ riboswitch case study

As mentioned above, different variants of the BHG-HMMs can be constructed by choosing a combination of the three user-defined parameters: the number of bins, b , used to group the FRET values, the time-scalar, c_0 , used to gauge the time axes in Eqn. 1 and the noise level, Δ , used to perturb distributions of *in silico* distances and their resulting emission probabilities. A naïve method for model selection is to evaluate the quality of each BHG-HMM according to the sum of the Viterbi scores over all the input FRET traces and then to choose the model with the maximal value.

In principle, one could try as many combinations of the BHG-HMM parameters as possible, however, this is computationally demanding and not necessary since in practice many parameter combinations give rise to similar results. For this reason, we limited ourselves to a fixed number of sparse parameter combinations: We set the number of

bins b to be either 5 or 10, the noise level Δ to be 0, 10 Å or 15 Å, and used 4 values for the time-scalar c_0 for the *Bsu* preQ₁ riboswitch. Further, it is not ideal to compare BHG-HMMs with different numbers of bins because, when there are more emission states, the emission probabilities get lower and so is the overall likelihood for a particular trace.

Thus, we analyzed our two RNAs following the two-step strategy illustrated in Fig. 2. First, without adding noise, we grouped the parameter combinations into the two categories according to the number of bins. Then for each category, only the optimal BHG-HMM with the highest Viterbi score was selected for the second step of a robustness analysis. In the second step, input FRET traces were further analyzed with **FRETtranslator** using noise-perturbed variants of the original optimal BHG-HMMs to extract robust structural information. In other words, we aim at identical predictions that disregard changes in noise levels. In this step, we considered two levels of added noise: $\Delta = 10$ and 15 Å.

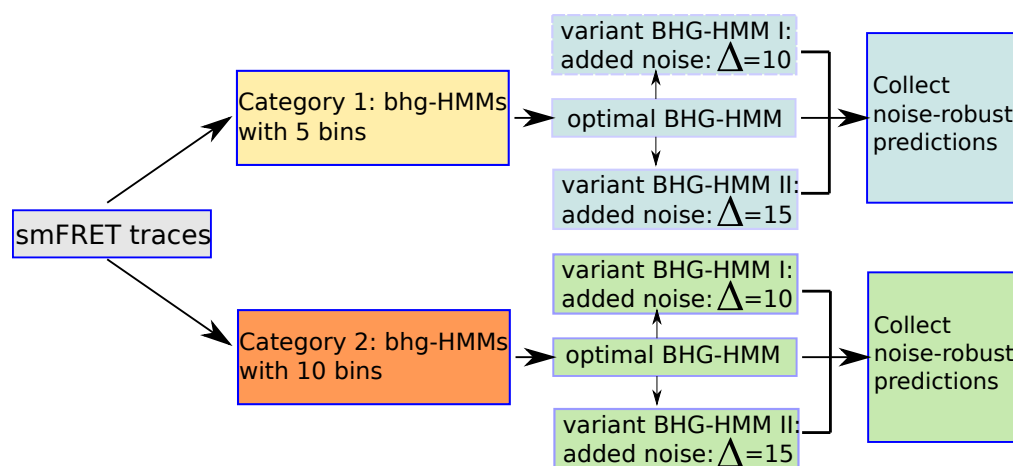


Fig 2. Work flow in case study. We analyzed our two examples according to a two-step strategy: First, without adding noise, we grouped the parameter combinations into two categories according to the number of bins. Then for each category, only the optimal BHG-HMM with the highest Viterbi score was selected for the second step featuring a more robust analysis. In this second step, input FRET traces were further analyzed with **FRETtranslator** using noise-perturbed variants of the original optimal BHG-HMMs to extract robust structural information. In this step, we considered two levels of added noise, 10 and 15 Å.

Data preparation for the *Bsu* preQ₁ riboswitch case study.

Preparation of RNAs for smFRET.

The 36-nt *Bsu* RNA construct was synthesized by Dharmacon Inc. containing a 5-biotin modification for immobilization, a 3'DY547 fluorescent label, and a 5' aminoallyl-uridine (5-N-U) at position U13 for functionalization with Cy5 (Table 1) [19]. Upon deprotection, 3.4 nmol RNA was incubated with one dye pack of Cy5-HNS ester (GE Healthcare) dissolved in 30 μ l DMSO in a total reaction volume of 50 μ l containing 0.1 M sodium bicarbonate buffer (pH 8.7). Reactions were allowed to proceed at room temperature for 4 h before dilution to 500 μ l with water and purification on a Nap-5 gel filtration column (GE Healthcare). Fractions containing the labeled RNA were collected and ethanol precipitated.

Table 1. Sequence information for the *Bsu* preQ₁ riboswitch case study.

5'-AGAGGUUCUAGC (5-N-U) ACACCCUCUAUAAAAACUAAGG (DY547)-3'

The *Bsu* preQ₁ riboswitch was synthesized with the Dy547 fluorophore on its 3' end to serve as the donor fluorophore. The allyl-amine modified uridines utilized for labeling is denoted as (5-N-U) with red representing positioning of the acceptor fluorophore.

smFRET analysis of RNA constructs.

smFRET analysis of the *Bsu* preQ₁ riboswitch RNA was performed as previously described in [19]. Briefly, the RNA was folded by heating at 70 °C for 2 min and allowing it to cool to room temperature (RT) for at least 20 min in smFRET buffer (50 mM Tris-HCl (pH 7.5), 100 mM KCl) in the presence of 100 nM preQ₁. Folded RNA was flowed onto a quartz slide coated with biotinylated-BSA and streptavidin and allowed to incubate for 10 min for binding. Excess RNA was removed by washing with 200 μ l of smFRET buffer with preQ₁. smFRET was carried out using a prism-based TIRF microscope, a 532-nm laser to excite the donor (Cy3), and a 635-nm laser to excite the acceptor (Cy5) with the emission recorded at 100 ms time resolution with a Princeton Instruments, I-PentaMAX intensified CCD camera. Data were collected in the presence of the smFRET buffer containing an oxygen scavenging system (OSS) composed of protocatechuate dioxygenase, protocatechuate and Trolox by directly exciting Cy3 and recording of both Cy3 and Cy5 emission intensities. Following molecule selection, the *k*-means algorithm in the QuB software suite was utilized for HMM analysis using a two-state model to idealize the data. This data set contained in total 150 smFRET traces. All FRET values are rounded to two decimal digits.

BHG-HMM construction for FRETtranslator.

To obtain the hidden states, we first generated the BHG of the *Bsu* preQ₁-riboswitch with methods provided in [30] using the parameter -k, indicating that pseudoknotted structures are taken into consideration. Only the LMs with negative energies in the resulting BHG were selected since they are thermodynamically favorable. This left just four candidate structures. We emphasize that each candidate structure as an LM represents a basin (ensemble) of structures in the RNA folding landscape. The initial probabilities of the four candidate structures were computed according to the Boltzmann distribution as previously described. Due to the lack of experimental data to determine the BHG time-scalar c_0 , we computed in total four different sets of transition probabilities with $c_0 \in \{10, 10^2, 10^3, 10^4\}$ and $t = 0.1$ seconds according to Eqn. 1. Note that the transition probabilities stay the same as the initial probabilities when $c_0 > 10^4$ since the system reaches thermodynamic equilibrium.

The emission probability for each candidate structure is estimated based on a set of $\geq 350,000$ *in silico* generated 3D structures from Ernwin in order to make sure the sampling is sufficient.

Without considering the added noise, a total of 8 BHG-HMMs were generated from different parameter combinations for further data analysis with FRETtranslator.

Results

We applied our method to a 36-nt *Bsu* preQ₁ riboswitch. This RNA is known to preferentially adopt a pseudoknot structure upon binding of a preQ₁ ligand. Previous smFRET studies [19] have revealed a relative shift in FRET states from a partially folded conformation with a moderate FRET value of ~ 0.6 in the absence of the ligand

to a fully folded conformation with a high FRET value of ~ 0.9 in the presence of ligand. Through biochemical and computational analysis, these FRET conformations were shown to correspond to hairpin and pseudoknotted structures, respectively [19].

As shown in Figs. 3 and 4, the computed BHG-HMM of this RNA contains four candidate structures. These structures are indexed according to their free energies in ascending order. Given that we only consider canonical base pairs, structure 1 matches the low-FRET hairpin structure whereas the base pairs of structure 4 are consistent with the previously determined pseudoknotted high-FRET structure [19]. The initial and transition probabilities between these structures are shown in Fig. 3, wherein the transition probabilities are calculated when the BHG time-scalar $c_0 = 10$. As shown in Fig. 4, the emission probabilities of candidate structures are estimated based on a large set of structures sampled with **Ernwin**. The emission probabilities of structure 1, 2 and 3 share a similar pattern whereas the emission probabilities of structure 4 are dominated by high FRET values.

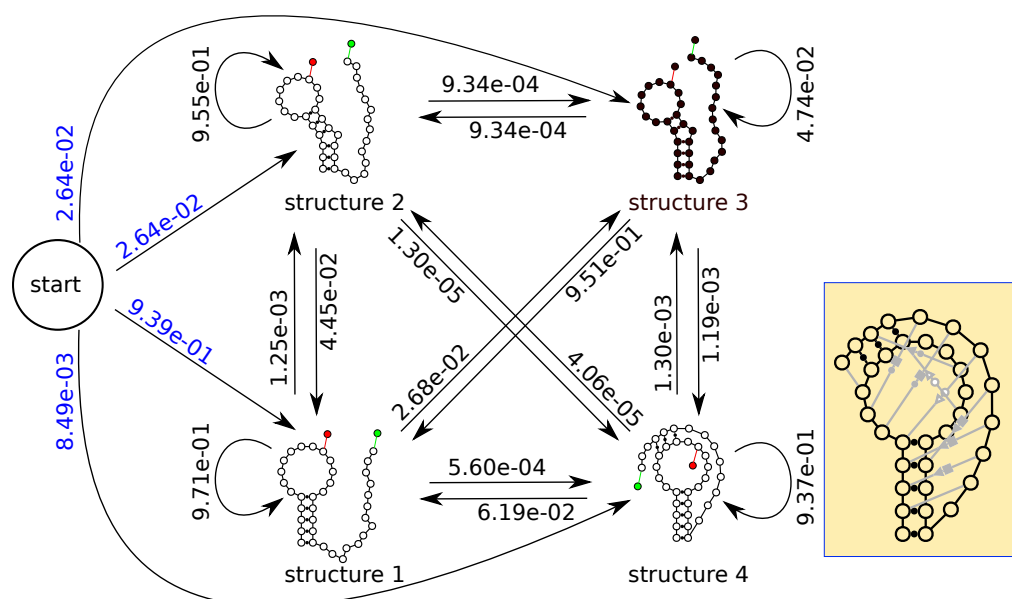


Fig 3. Hidden states, initial probabilities and transition probabilities of a BHG-HMM constructed for the preQ₁ riboswitch. Red and green markers indicate the locations of donors and acceptors, respectively. Arrows indicate possible transitions. The numbers in blue and black are the initial and transition probabilities, respectively. The transition probabilities are calculated with a BHG time-scalar $c_0 = 10$. The previously determined native structure in the ligand-bound state [19] is indicated with a yellow background for comparison. Non-canonical base pairs in the native structure, which are not considered in the BHG model, are colored in grey. All diagrams of RNA secondary structures are plotted with RNAfold [44].

FRETtranslator is applied to decode all 150 smFRET traces independently according to all 8 BHG-HMMs initially derived. In this step, no noise is added for estimating the emission probabilities. In general, as shown in Table 2, when the BHG time-scalar $c_0 = 10, 10^2, 10^3$, structural transitions between structures 1 and 4 are predicted to dominate. Such transitions occupy $\geq 96.5\%$ of the overall predicted transitions. Transitions between structures 1 and 2 are observed as well, but relatively rarely. When c_0 increases to 10^4 , no structural transition is observed, as for all time stamps among all traces the RNA is predicted to stay in structure 1. This is because the transition probability from structure 4 to itself exhibits a sharp drop from $\geq 92\%$ to $\sim 1\%$. In

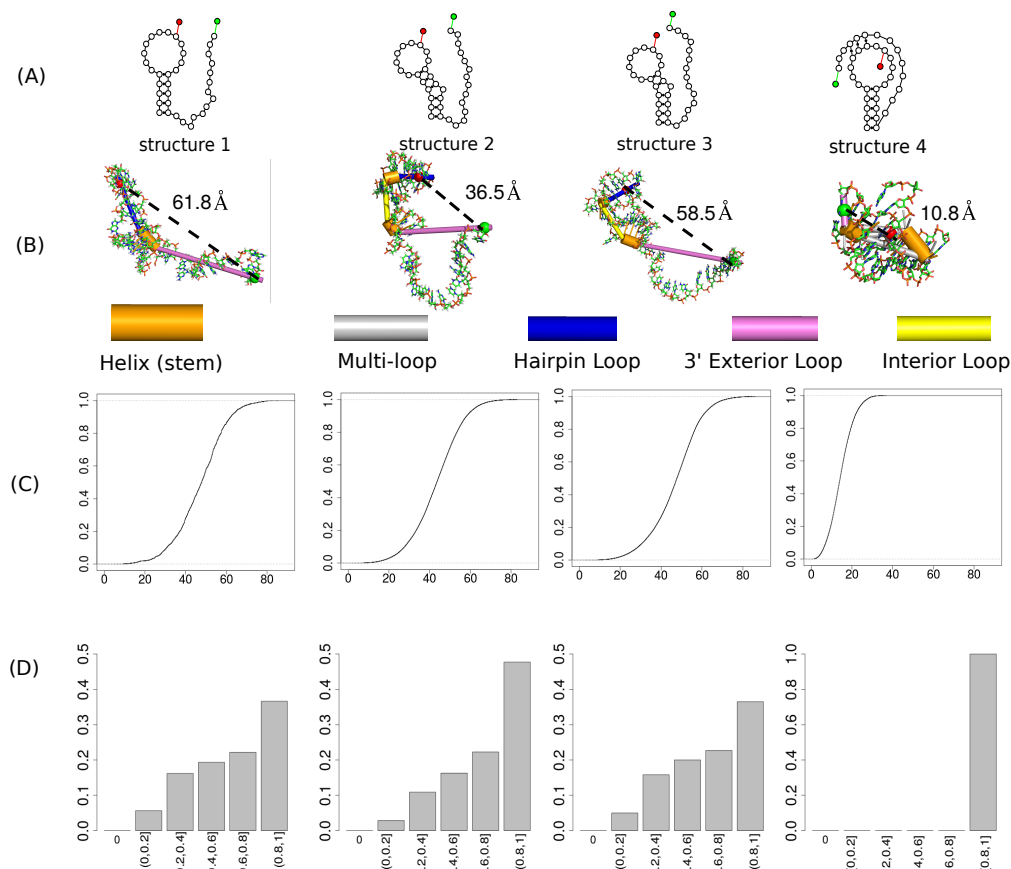


Fig 4. Emission probabilities of a BHG-HMM constructed for the preQ₁ riboswitch. (A) Four candidate structures, where red and green markers indicate the nucleotide locations of the donor (C13) and acceptor fluorophores (G36), respectively. (B) Examples of *in silico* generated 3D structures with **Ernwin** are displayed below their corresponding secondary structures. The structural elements in use are indicated below these structures. (C) The empirical cumulative distribution function of the *in silico* distances for each candidate structure. (D) The emission probabilities are converted from *in silico* distances estimated with **Ernwin**. The nonzero FRET values are grouped into 5 bins and an extra bin for value 0. Each bar indicates the emission probability of a bin, which is essentially an interval of FRET-values as labeled in the figure.

the meanwhile, the transition probability from structure 4 to structure 1 increases from $\leq 8\%$ to 94%. Thus, when $c_0 = 10^4$, instead of staying in structure 4, molecule prefers to quickly fold into its most stable structure, i.e., structure 1. That is, the molecule tends to stay in structure 1 rather than to transit to another structure.

According to their Viterbi scores, two optimal BHG-HMMs (highlighted in blue in Table 2) are selected from the groups of BHG-HMMs based on bin sizes $b = 5$ or $b = 10$. For each optimal model, two levels of noise $\Delta = 10\text{\AA}$ and 15\AA are added to perturb the emission probabilities for testing their robustness in a second round of predictions. Fig. 5 summarizes the structural transitions predicted with **FRETtranslator** in this second round, using the optimal first-round BHG-HMMs and their noise-added variants.

We observed that adding noise has two effects on the results. First, it reduces the total number of transitions predicted with **FRETtranslator** ($\leq 15\%$). In fact, the larger the value of Δ is, the fewer transitions are observed. This is mainly because added noise

Table 2. Numbers of structural transitions predicted for the preQ₁ riboswitch with different BHG-HMMs without added noise. Different BHG-HMMs are defined based on BHG time-scalar c_0 (first column) and the number of bins b (second column). Values listed in column 3, 4, 5 and 6 are the percentages of the overall predicted transitions which are given in column 7. The overall ranking of the combinations of parameters based on their Viterbi scores are shown in the last column. Two optimal BHG-HMMs are highlighted in blue.

$\log(c_0)$	b	1→4 (%)	4→1 (%)	1→2 (%)	2→1 (%)	Total number of transitions	Ranking
1	5	48.4	48.8	1.6	1.3	2608	2
1	10	48.5	49.1	1.2	0.1	2645	5
2	5	48.9	49.2	1.0	1.0	2980	1
2	10	48.0	48.5	1.8	1.7	2947	4
3	5	49.3	49.6	0.6	0.5	3604	3
3	10	48.1	48.6	1.7	1.7	2963	6

changes the emission probability distributions of structure 4 for the bins containing high FRET values. When no noise is added, the emission probability of structure 4 is nonzero only for the bins with FRET values in the range of (0.8, 1] when $b = 5$ and (0.9, 1] when $b = 10$. Secondly, noise reduces the number of transitions predicted between structures 1 and 2. Further, it substantially (by $\geq 60\%$) reduces the total number of occurrences of structure 2 as a predicted structure. This is mainly because noise decreases the emission probabilities of structure 2 for FRET values lying in the range of (0.4, 0.9].

Given that noise naturally causes differences, we further sought to identify predictions that are noise-robust. In particular, when the number of bins is fixed, we only consider the predictions that are reported by all three cases: the optimal BHG-HMM and its two noise-added variants at noise levels 10 and 15 Å. We summarize the noise-robust structural transitions in Table 3. In general, transitions between structures 1 and 4 are dominant ($\geq 99.0\%$). When $b = 5$ and $b = 10$ only one and 22 transitions, respectively, are predicted between structures 1 and 2.

Table 3. Numbers of noise-robust structural transitions predicted for the preQ₁ riboswitch. Values listed in column 2, 3, 4 and 5 are the percentages of the overall robust predicted transitions which are given in column 6. These values are derived using noise-perturbed variants of the two optimal BHG-HMMs highlighted in Table 2.

b	1→4 (%)	4→1 (%)	1→2 (%)	2→1 (%)	Total number of noise-robust transitions
5	49.9	50.0	0.1	0.0	2630
10	49.3	49.8	0.5	0.4	2501

Fig. 6 shows the compositions of predicted structures for each bin determined FRET-value interval based on the optimal BHG-HMMs. In addition, we show the compositions that are noise-robust. First, FRET values collected from all 150 input FRET traces range from 0.46 to 0.98. The high FRET values appear more frequent than the low FRET values. When $b = 5$, using the optimal BHG-HMM, structures 1 and 4 completely occupy the lower FRET-values within range (0.4, 0.6] and higher FRET-values within (0.8, 1], respectively. Structure 2 is observed often (29.8%) but still much less frequently than structure 1 (70.2%) for the FRET-values within (0.6, 0.8]. This is mainly because the emission probability for structure 2 corresponding to FRET-value interval (0.6, 0.8] is the maximum among all candidate structures. Thus, for an input trace with FRET values lying only within (0.6, 0.8], FRETtranslator has a tendency to assign structure 2 to the entire trace. This is why not many predicted structural transitions involve structure 2 while a largely static structure 2 still occupies a portion in the overall composition. Only a small fraction (8.8%) of these structure 2 predictions is noise-robust since the added noise weakens the privilege of structure 2 regarding emission probabilities.

When $b = 10$, using the optimal BHG-HMM, structures 1 and 4 dominantly occupy

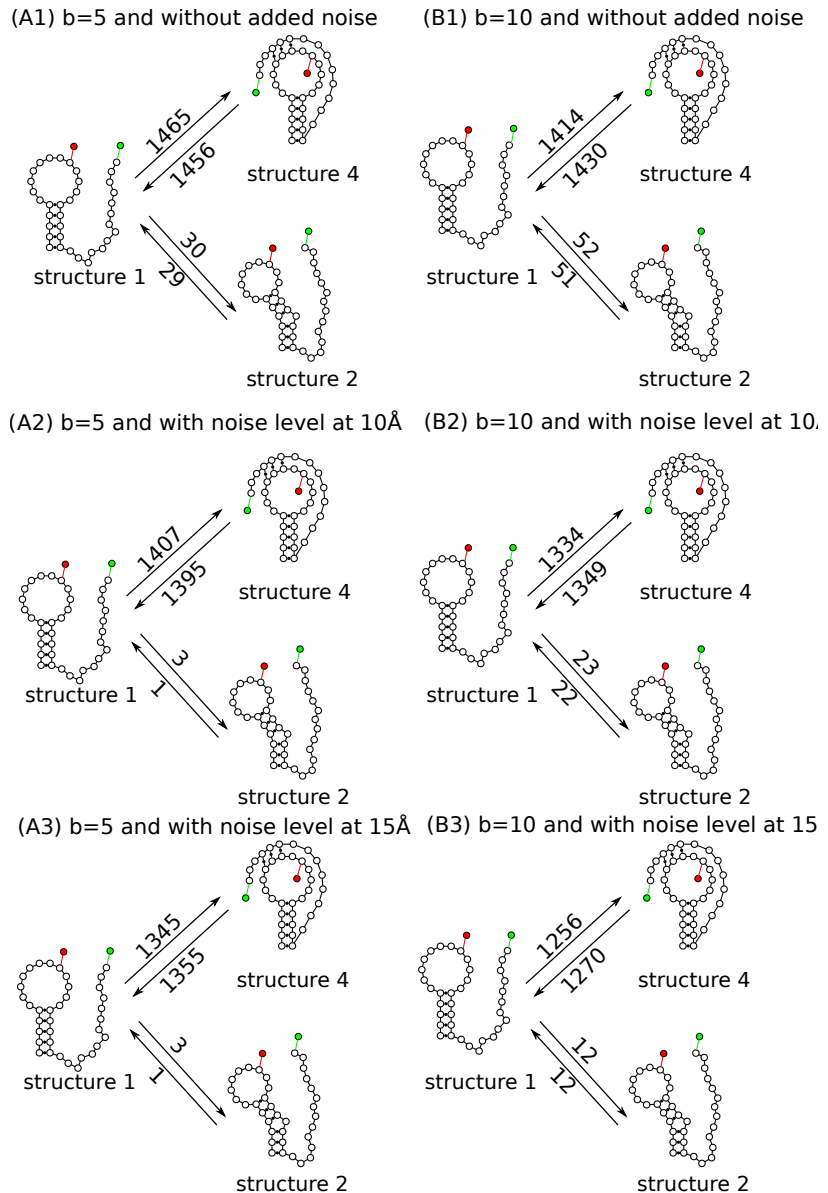


Fig 5. Structural transition predictions for the preQ₁ riboswitch using the optimal BHG-HMMs from the first round and their noise-added variants. (Left) Optimal BHG-HMM with $b = 5$ (A1) and two noise-added variants: using noise level $\Delta = 10\text{\AA}$ (A2) and $\Delta = 15\text{\AA}$ (A3). (Right) Optimal BHG-HMM with $b = 10$ (B1) and two noise-added variants: using noise level $\Delta = 10\text{\AA}$ (B2) and $\Delta = 15\text{\AA}$ (B3). Structural transitions are dominated by transitions between structure 1 and structure 4 comparing to transitions between structure 1 and structure 2. The added noise reduces the number of the transitions between structure 1 and structure 2.

the lower FRET-values within range $(0.4, 0.7]$ and higher FRET-values within $(0.9, 1]$, respectively. Structures 1 and 2 are predicted with similar frequencies for the FRET values within $(0.7, 0.8]$, with structure 2 being of a slightly lower frequency of $\sim 42.2\%$. Again only a small fraction of these structure 2 predictions is noise-robust, only $\sim 6.9\%$. All three structures are observed for FRET values within $(0.8, 0.9]$ while structures 2 and 4 are predicted much more often than structure 1. Furthermore, structure 2 is

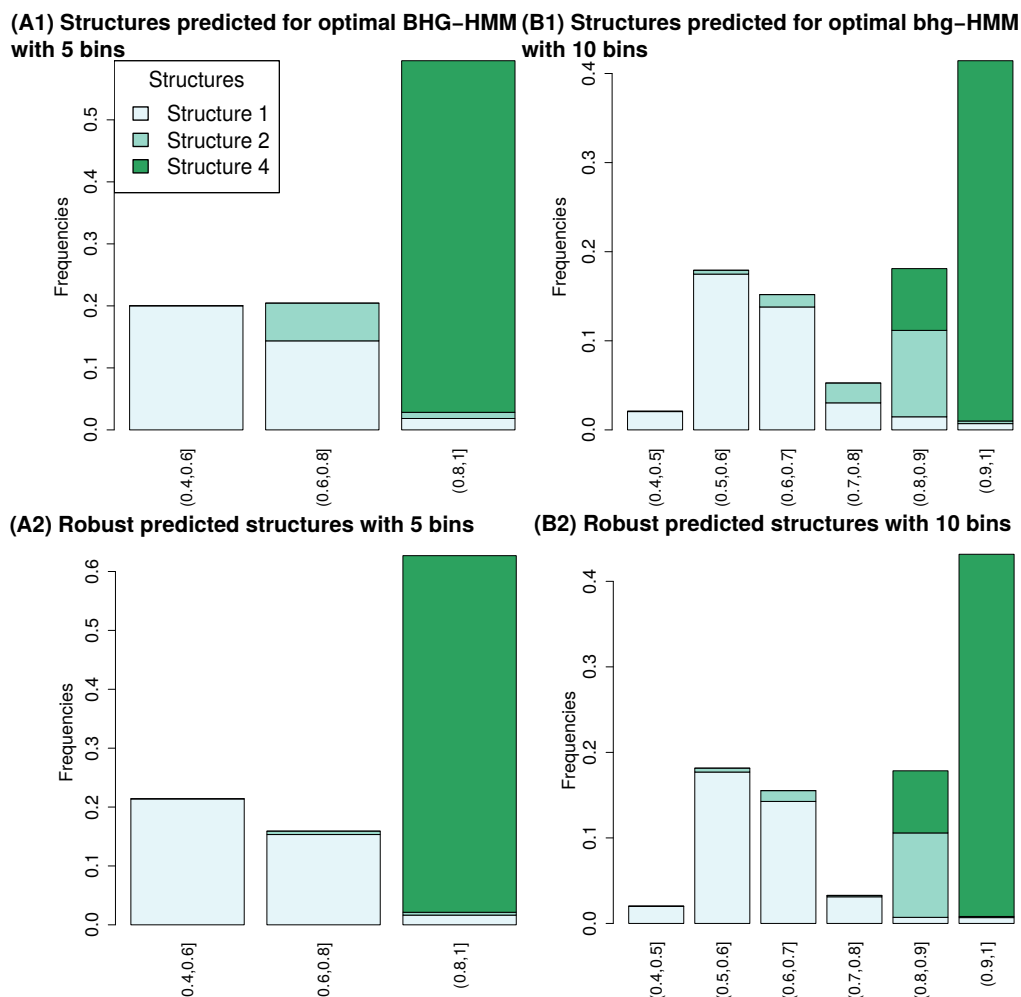


Fig 6. The compositions of predicted structures for all bin-determined FRET-value intervals. When the numbers of bins are $b = 5$ and $b = 10$, the compositions of predicted structures for each bin-determined FRET-value interval using the optimal BHG-HMMs are shown in (A1) and (B1), respectively. Furthermore, analogous compositions of predicted structures, which are robust against added noise, are provided in (A2) and (B2), respectively. The frequencies of FRET-value intervals are indicated in the y-axes. Colors are used to distinguish different predicted structures as indicated. Only the bin-determined intervals with non-zero frequencies are shown.

most frequently observed ($\sim 53.6\%$) for this FRET-value interval, and the prediction regarding this FRET-interval is relatively noise-robust.

In summary, using a robust two-step analysis, our predictions with **FRETtranslator** show the following: (1) structural transitions are most likely observed between structures 1 and 4, while transitions between structure 1 and structure 2 are rarely observed; (2) Independent of the choices of the number of bins, structures 1 and 4 dominate the FRET values within $(0.4, 0.8]$ and $(0.9, 1]$, respectively; (3) For the FRET values within $(0.8, 0.9]$, when $b = 5$, **FRETtranslator** suggests structure 4 is most likely, while both structures 2 and 4 are suggested when $b = 10$. Given that the prediction of structure 2 is sensitive to the chosen number of bins, we are more confident with the structure 4 predictions. Thus, the results of our method are consistent with a previous analysis [19], wherein structure 1 as the hairpin-like structure was assigned to all low-FRET values

and structure 4 as the pseudoknotted structure was assigned to all high-FRET values.

Discussion

FRETtranslator is a Viterbi-decoding approach for predicting RNA structural pathways based on smFRET traces, the analysis of RNA secondary structure landscapes, and 3D structure prediction. **FRETtranslator** only requires smFRET traces and the RNA sequence as input. To our knowledge, this is the first method that is capable of directly translating an input smFRET trace into a folding trajectory of secondary structures. We apply our method to the preQ₁ riboswitch example. The results are consistent with previous analysis provided in [19], wherein the hairpin-like structure and the pseudoknotted structure are assigned to all low-FRET values and all high-FRET values, respectively.

The performance of **FRETtranslator** depends on the accuracies of its three elementary parts: RNA folding landscape analysis, RNA 3D-structure sampling and the quality of the smFRET traces.

The RNA folding landscape defines the candidate secondary structures that we can assign to time points in the smFRET traces. In this study, we use basin hopping graph (BHG) to coarse grain the folding landscape. Vertices in BHG correspond to the “basins” in the landscape and are represented by the LM structure at the bottom of the basin. While it would be ideal to use the entire set of LMs, this is computationally infeasible given the number LMs grows as the square root of the number of structures [45]. To overcome this limitation, in this study we consider only the low-energy part of the landscape by restricting the energy of structures within certain threshold. In future work, we might avoid selecting LMs sharing very similar structural elements. Existing methods, for instance RNASHapes [46] and RNAgraphdist [47] can be promising.

In our method, the 3D sampling software in choice determines the quality of the estimated emission probability and thus also the performance of the **FRETtranslator**. **Ernwin** [29] is to our best knowledge the only coarse-grained fragment-assembly approach has ability to generate ensembles of structures competitive with the predictions of more sophisticated all-atom models such as FARNAs [48]. Typical all-atom approaches to the prediction of RNA 3D structure yield modest accuracy for smaller molecules but suffer from extremely low accuracy for any structure beyond ~30 nt in length. Other recently developed coarse-grained approaches, e.g. SimRNA [49] are also promising however only one optimal structure is provided. The prediction accuracy can likely be improved if more experimental data regarding structural element can be included: as the existence of pseudoknots as the case for the preQ₁ riboswitch.

Given the recent development of tools for RNA secondary structure prediction to integrate chemical probing data such as footprinting reactivities [50–53], the current RNA secondary structure sampling during the BHG computation could be extended to take footprinting data into account. This could potentially improve the performance of **FRETtranslator** predictions. However, incorporating chemical probing data is not a trivial task. For example, several different structures could each show little overlap with the chemical probing data, but match the reactivities as an ensemble of structures. The emerging MCM [27] approaches, however, hold the promise to disentangle at least the most prevalent alternative conformations.

The performance of **FRETtranslator** furthermore depends on the design of the smFRET experiment itself. This includes the locations of donor and the acceptor fluorophores, the FRET signal and its pre-processing. Inter-fluorophore distances should effectively reflect the structural changes. Also, the method used for idealizing FRET values can potentially have a large impact on the predictions. At least we suggest, the number of FRET states selected in idealizing raw FRET values should be the same as

the number of bins used in selecting BHG-HMMs. In addition, the way that traces are split is also delicate. For instance, if the pre-processing of raw FRET efficiencies yields traces that only contain a single value it is less likely that our method performs well. After all, the strength of **FRETtranslator** is in analyzing transitions between structures.

Finally, the Viterbi model, which **FRETtranslator** is based on, has its shortcoming as it focuses on a single path. Similar to alternative structures, there will also be alternative paths. In our future study, we hint at considering posterior decoding as a possible improvement of our method.

Supporting Information

S1 Text. RNA folding landscapes and basin hopping graphs.

S2 Text. Measuring the *in silico* inter-fluorophore distance with Ernwin.

Acknowledgments

We thank Dr. Krishna Suddala for providing smFRET data of the preQ₁ riboswitch. Also many thanks to Dr. Marcel Kucharik for computing basin hopping graphs for the preQ₁ riboswitch.

Author Contributions

PFS, ILH, JG, NGW and JQ conceived and designed the experiments. MLK performed the smFRET experiments. NH, PK and JQ performed computational analysis. NH, MLK, PK, NGW and JQ analyzed the data. All coauthors contributed reagents/materials/analysis tools and wrote the paper together.

Funding Information

Austrian Science Fund (FWF): [M1618-N28] to JQ. Deutsche Forschungs Gemeinschaft STA 850/15-1 to PFS. The Lundbeck Foundation, Innovation Fund Denmark to JG, US National Institutes of Health grant R01GM098023 to NGW.

References

1. Haller A, Souliere MF, Micura R. The dynamic nature of RNA as key to understanding riboswitch mechanisms. *Acc Chem Res.* 2011;44(12):1339–48. doi:10.1021/ar200035g.
2. Liberman JA, Suddala KC, Aytenfisu A, Chan D, Belashov IA, Salim M, et al. Structural analysis of a class III preQ₁ riboswitch reveals an aptamer distant from a ribosome-binding site regulated by fast dynamics. *Proc Natl Acad Sci U S A.* 2015;112(27):E3485–94. doi:10.1073/pnas.1503955112.
3. Suddala KC, Wang J, Hou Q, Walter NG. Mg(2+) Shifts Ligand-Mediated Folding of a Riboswitch from Induced-Fit to Conformational Selection. *J Am Chem Soc.* 2015;137(44):14075–83. doi:10.1021/jacs.5b09740.

4. Rinaldi AJ, Lund PE, Blanco MR, Walter NG. The Shine-Dalgarno sequence of riboswitch-regulated single mRNAs shows ligand-dependent accessibility bursts. *Nat Commun.* 2016;7:8976. doi:10.1038/ncomms9976.
5. Chowdhury S, Maris C, Allain FH, Narberhaus F. Molecular basis for temperature sensing by an RNA thermometer. *Embo j.* 2006;25(11):2487–97. doi:10.1038/sj.emboj.7601128.
6. Zhuang X, Kim H, Pereira MJ, Babcock HP, Walter NG, Chu S. Correlating structural dynamics and function in single ribozyme molecules. *Science.* 2002;296(5572):1473–6. doi:10.1126/science.1069013.
7. Rhodes MM, Reblova K, Sponer J, Walter NG. Trapped water molecules are essential to structural dynamics and function of a ribozyme. *Proc Natl Acad Sci U S A.* 2006;103(36):13380–5. doi:10.1073/pnas.0605090103.
8. Abelson J, Blanco M, Ditzler MA, Fuller F, Aravamudhan P, Wood M, et al. Conformational dynamics of single pre-mRNA molecules during in vitro splicing. *Nat Struct Mol Biol.* 2010;17(4):504–12. doi:10.1038/nsmb.1767.
9. Krishnan R, Blanco MR, Kahlscheuer ML, Abelson J, Guthrie C, Walter NG. Biased Brownian ratcheting leads to pre-mRNA remodeling and capture prior to first-step splicing. *Nat Struct Mol Biol.* 2013;20(12):1450–7. doi:10.1038/nsmb.2704.
10. Blanco MR, Martin JS, Kahlscheuer ML, Krishnan R, Abelson J, Laederach A, et al. Single Molecule Cluster Analysis dissects splicing pathway conformational dynamics. *Nat Methods.* 2015;12(11):1077–84. doi:10.1038/nmeth.3602.
11. Xu X, Yu T, Chen SJ. Understanding the kinetic mechanism of RNA single base pair formation. *Proc Natl Acad Sci U S A.* 2016;113(1):116–21. doi:10.1073/pnas.1517511113.
12. Wu Y, Shi B, Ding X, Liu T, Hu X, Yip KY, et al. Improved prediction of RNA secondary structure by integrating the free energy model with restraints derived from experimental probing data. *Nucleic Acids Res.* 2015;43(15):7247–59. doi:10.1093/nar/gkv706.
13. Salmon L, Bascom G, Andricioaei I, Al-Hashimi HM. A general method for constructing atomic-resolution RNA ensembles using NMR residual dipolar couplings: the basis for interhelical motions revealed. *J Am Chem Soc.* 2013;135(14):5457–66. doi:10.1021/ja400920w.
14. Sloma MF, Mathews DH. Improving RNA secondary structure prediction with structure mapping data. *Methods Enzymol.* 2015;553:91–114. doi:10.1016/bs.mie.2014.10.053.
15. Todd GC, Walter NG. Secondary structure of bacteriophage T4 gene 60 mRNA: implications for translational bypassing. *Rna.* 2013;19(5):685–700. doi:10.1261/rna.037291.112.
16. Joo C, Balci H, Ishitsuka Y, Buranachai C, Ha T. Advances in single-molecule fluorescence methods for molecular biology. *Annu Rev Biochem.* 2008;77:51–76. doi:10.1146/annurev.biochem.77.070606.101543.
17. Roy R, Hohng S, Ha T. A practical guide to single-molecule FRET. *Nat Methods.* 2008;5(6):507–16. doi:10.1038/nmeth.1208.

18. Lemay JF, Penedo JC, Tremblay R, Lilley DM, Lafontaine DA. Folding of the adenine riboswitch. *Chem Biol*. 2006;13(8):857–68. doi:10.1016/j.chembiol.2006.06.010.
19. Suddala KC, Rinaldi AJ, Feng J, Mustoe AM, Eichhorn CD, Liberman JA, et al. Single transcriptional and translational preQ1 riboswitches adopt similar pre-folded ensembles that follow distinct folding pathways into the same ligand-bound structure. *Nucleic Acids Res*. 2013;41(22):10462–75. doi:10.1093/nar/gkt798.
20. Bronson JE, Fei J, Hofman JM, Gonzalez J R L, Wiggins CH. Learning rates and states from biophysical time series: a Bayesian approach to model selection and single-molecule FRET data. *Biophys J*. 2009;97(12):3196–205. doi:10.1016/j.bpj.2009.09.031.
21. Qin F, Li L. Model-based fitting of single-channel dwell-time distributions. *Biophys J*. 2004;87(3):1657–71. doi:10.1529/biophysj.103.037531.
22. Keller BG, Kobitski A, Jaschke A, Nienhaus GU, Noe F. Complex RNA folding kinetics revealed by single-molecule FRET and hidden Markov models. *J Am Chem Soc*. 2014;136(12):4534–43. doi:10.1021/ja4098719.
23. Feng J, Walter NG, Brooks r C L. Cooperative and directional folding of the preQ1 riboswitch aptamer domain. *J Am Chem Soc*. 2011;133(12):4196–9. doi:10.1021/ja110411m.
24. Ditzler MA, Otyepka M, Sponer J, Walter NG. Molecular dynamics and quantum mechanics of RNA: conformational and chemical change we can believe in. *Acc Chem Res*. 2010;43(1):40–7. doi:10.1021/ar900093g.
25. Laing C, Schlick T. Computational approaches to RNA structure prediction, analysis, and design. *Curr Opin Struct Biol*. 2011;21(3):306–18. doi:10.1016/j.sbi.2011.03.015.
26. Magnus M, Matelska D, Lach G, Chojnowski G, Boniecki MJ, Purta E, et al. Computational modeling of RNA 3D structures, with the aid of experimental restraints. *RNA Biol*. 2014;11(5):522–36. doi:10.4161/rna.28826.
27. Tian S, Das R. RNA structure through multidimensional chemical mapping. *Quarterly Review of Biophysics*. 2016;doi:http://dx.doi.org/10.1101/038679.
28. Kucharik M, Hofacker IL, Stadler PF, Qin J. Basin Hopping Graph: a computational framework to characterize RNA folding landscapes. *Bioinformatics*. 2014;30(14):2009–17. doi:10.1093/bioinformatics/btu156.
29. Kerpedjiev P, Honer Zu Siederdisen C, Hofacker IL. Predicting RNA 3D structure using a coarse-grain helix-centered model. *Rna*. 2015;21(6):1110–21. doi:10.1261/rna.047522.114.
30. Kucharik M, Hofacker IL, Stadler PF, Qin J. Pseudoknots in RNA folding landscapes. *Bioinformatics*. 2015;doi:10.1093/bioinformatics/btv572.
31. T WM, A SSW, C F, L HI, F SP. Exact folding dynamics of RNA secondary structures. *J Phys A: Math Gen*. 2004;37:4731–4741.
32. Reidys CM, Huang FW, Andersen JE, Penner RC, Stadler PF, Nebel ME. Topology and prediction of RNA pseudoknots. *Bioinformatics*. 2011;27(8):1076–85. doi:10.1093/bioinformatics/btr090.

33. Zuker M. Mfold web server for nucleic acid folding and hybridization prediction. *Nucleic Acids Res.* 2003;31(13):3406–15.
34. Lorenz R, Bernhart SH, Honer Zu Siederdisen C, Tafer H, Flamm C, Stadler PF, et al. ViennaRNA Package 2.0. *Algorithms Mol Biol.* 2011;6:26. doi:10.1186/1748-7188-6-26.
35. Mathews DH, Sabina J, Zuker M, Turner DH. Expanded sequence dependence of thermodynamic parameters improves prediction of RNA secondary structure. *J Mol Biol.* 1999;288(5):911–40. doi:10.1006/jmbi.1999.2700.
36. Andronescu M, Condon A, Hoos HH, Mathews DH, Murphy KP. Efficient parameter estimation for RNA secondary structure prediction. *Bioinformatics.* 2007;23(13):i19–28. doi:10.1093/bioinformatics/btm223.
37. Hofacker IL, Schuster P, Stadler PF. Combinatorics of RNA secondary structures. *Discrete Applied Mathematics.* 1998;88(1–3):207–237. doi:http://dx.doi.org/10.1016/S0166-218X(98)00073-0.
38. Blanco M, Walter NG. Analysis of complex single-molecule FRET time trajectories. *Methods Enzymol.* 2010;472:153–78. doi:10.1016/s0076-6879(10)72011-5.
39. Foester T. *Fluoreszenz Organisher Verbindungen.* Goettingen: Vandenhoeck and Ruprecht; 1951.
40. Pereira MJ, Nikolova EN, Hiley SL, Jaikaran D, Collins RA, Walter NG. Single VS ribozyme molecules reveal dynamic and hierarchical folding toward catalysis. *J Mol Biol.* 2008;382(2):496–509. doi:10.1016/j.jmb.2008.07.020.
41. Kalinin S, Peulen T, Sindbert S, Rothwell PJ, Berger S, Restle T, et al. A toolkit and benchmark study for FRET-restrained high-precision structural modeling. *Nat Methods.* 2012;9(12):1218–25. doi:10.1038/nmeth.2222.
42. Forney J G D. The viterbi algorithm. *Proceedings of the IEEE.* 1973;61(3):268–278. doi:10.1109/PROC.1973.9030.
43. Lott PC, Korf I. StochHMM: a flexible hidden Markov model tool and C++ library. *Bioinformatics.* 2014;30(11):1625–6. doi:10.1093/bioinformatics/btu057.
44. Hecker N, Wiegels T, Torda AE. RNA secondary structure diagrams for very large molecules: RNAfdl. *Bioinformatics.* 2013;29(22):2941–2. doi:10.1093/bioinformatics/btt496.
45. Lorenz WA, Clote P. Computing the partition function for kinetically trapped RNA secondary structures. *PLoS One.* 2011;6(1):e16178. doi:10.1371/journal.pone.0016178.
46. Janssen S, Giegerich R. The RNA shapes studio. *Bioinformatics.* 2015;31(3):423–5. doi:10.1093/bioinformatics/btu649.
47. Qin J, Fricke M, Marz M, Stadler PF, Backofen R. Graph-distance distribution of the Boltzmann ensemble of RNA secondary structures. *Algorithms Mol Biol.* 2014;9:19. doi:10.1186/1748-7188-9-19.
48. Das R, Baker D. Automated de novo prediction of native-like RNA tertiary structures. *Proc Natl Acad Sci U S A.* 2007;104(37):14664–9. doi:10.1073/pnas.0703836104.

49. Boniecki MJ, Lach G, Dawson WK, Tomala K, Lukasz P, Soltysinski T, et al. SimRNA: a coarse-grained method for RNA folding simulations and 3D structure prediction. *Nucleic Acids Res.* 2016;44(7):e63. doi:10.1093/nar/gkv1479.
50. Zarringhalam K, Meyer MM, Dotu I, Chuang JH, Clote P. Integrating chemical footprinting data into RNA secondary structure prediction. *PLoS One.* 2012;7(10):e45160. doi:10.1371/journal.pone.0045160.
51. Deigan KE, Li TW, Mathews DH, Weeks KM. Accurate SHAPE-directed RNA structure determination. *Proc Natl Acad Sci U S A.* 2009;106(1):97–102. doi:10.1073/pnas.0806929106.
52. Hajdin CE, Bellaousov S, Huggins W, Leonard CW, Mathews DH, Weeks KM. Accurate SHAPE-directed RNA secondary structure modeling, including pseudoknots. *Proc Natl Acad Sci U S A.* 2013;110(14):5498–503. doi:10.1073/pnas.1219988110.
53. Lorenz R, Luntzer D, Hofacker IL, Stadler PF, Wolfinger MT. SHAPE directed RNA folding. *Bioinformatics.* 2016;32(1):145–7. doi:10.1093/bioinformatics/btv523.